Structural anomaly and crystalline electric field excitations in low-dimensional KU_2Te_6

Mitchell M. Bordelon, Shannon S. Fender,* S. M. Thomas, Joe D. Thompson, Eric D. Bauer, and Priscila F. S. Rosa
Materials Physics and Applications—Quantum, Los Alamos National Laboratory, Los Alamos, New Mexico 87545, USA

(Received 30 March 2023; accepted 26 July 2023; published 8 August 2023)

Layered ternary actinide chalcogenides contain unique structural and magnetic properties that remain underexplored. KU_2Te_6 is a new member of the *A*-*R*-*Q* (*A* = alkali; *R* = actinide; *Q* = chalcogenide) materials family crystallizing in the *Cmcm* space group as part of the $CsTh_2Te_6$ structure type. Evidence of a structural anomaly appears near $T_s = 48$ K as a weak feature in specific heat and electrical resistivity. Magnetism in this material derives from local non-Kramers U^{4+} ions as suggested by charge balance and crystalline electric-field susceptibility analysis. These ions form one-dimensional U-U chains along the *a* axis, but do not exhibit signs of magnetic order to $T = 0.36$ K. The absence of magnetic order is consistent with the crystalline electric-field splitting of the U^{4+} $J = 4$ manifold into a series of nondegenerate singlets.

DOI: 10.1103/PhysRevB.108.064406

I. INTRODUCTION

Actinide chalcogenides often crystallize in unique structures and have interesting properties due to their $5f$ electron chemistry compounded with diversity in oxidation states and high coordination environments [1–7]. In particular, compounds containing uranium have been extensively studied due to their complex $5f$ electron states intertwined with neighboring ligand states within a variety of crystal structures that can lead to novel ground states. For instance, the binary U-*Q* (*Q* = O, S, Se, Te) form in multiple structure types and display complex interactions leading to (anti)ferromagnetism [8–11], hidden order multipolar states [12], and recently unconventional spin-triplet superconductivity in UTe_2 [13–19].

An integral component of these uranium-based quantum states is the single ion properties derived from local crystalline electric-field (CEF) effects [12,20]. The CEF effect often determines the size and symmetry for $5f$ uranium moments that incorporate into collective properties such as long-range magnetic order, electrical transport, and structural distortions. For example, the development of 3-**k** magnetic order in UO_2 results from complex CEF-driven quadrupolar interactions coupled to a structural distortion at $T_N = 31$ K [12,21]. The CEF effect is not limited to insulators and can be relevant in metallic materials with delocalized $5f$ states. In UM_2Si_2 (*M* = Pd, Ni, Ru, Fe), localized $5f^2$ states are relevant in magnetic and electronic states despite significant itinerant $5f^3$ character of the uranium atoms [22–25]. The $5f^2$ CEF generates a series of singlets, and the lowest-lying singlets couple to form a basis for antiferromagnetic order in *M* = Pd and Ni, hidden order in *M* = Ru, and Pauli-paramagnetism in *M* = Fe [22]. Similarly, the localized $5f^2$ CEF states of the superconductor UTe_2 likely account for the anisotropic magnetic susceptibility [17], but their role in pressure-induced antiferromagnetism remains unclear.

Directly studying uranium CEF states can be problematic because they are often obscured by strong Kondo and magnetic exchange interactions or metallicity [12,17,26–34]. One effective route to study uranium CEF states is to characterize insulating uranium-based materials with a well-defined valence leading to localized CEF levels. This condition is met in many of the ternary U-based materials within the chemical phase space between uranium, chalcogenide ions *Q*, and alkali ions *A* [35–45]. These materials host numerous complex crystal structures including alkali-metal intercalated uranium chalcogenides of the form A_2UQ_3 [35–37], $Cs_2U_3Se_7$ [38], $CsUTe_6$ [39], and AU_2Q_6 [40–45].

The most widely studied of these ternary materials reside in the AU_2Q_6 family, where two known structure types form: $CsTh_2Te_6$ type in space group *Cmcm* and KTh_2Se_6 type in space group *Immm* [40–45]. Typically, Te-based materials form in *Cmcm* while Se-based materials form in *Immm*. In both structure types, the $[RQ_3]$ parent structure adopts capped trigonal prismatic geometry surrounding the actinide ions, and dichalcogenide bonding results in a charge balance of $(A^+)_2(R^{4+})_4(Q^{2-})_6(Q_2^{2-})_3$ [43]. Both space groups contain interstitial *A* sites coordinated by eight *Q* ions but differ slightly in the stacking arrangement of $[RQ_3]$ two-dimensional layers. The *Cmcm* structure shifts neighboring $[RQ_3]$ layers by $1/2a$ while the *Immm* shifts $1/2(a + b)$ [43]. Within the $[RQ_3]$ layers, nearest-neighbor infinite U-U chains of roughly 4.0–4.3 Å form along the *a* axis [Fig. 1(a)].

Here, we report on a new member of the AU_2Q_6 family, KU_2Te_6, which crystallizes in the $CsTh_2Te_6$ *Cmcm* structure type, and determine its physical properties and CEF levels. Electrical resistivity shows insulating behavior in KU_2Te_6 to 2 K, in agreement with the charge balance above, and a weak structural transition near $T_s = 48$ K that is also present in specific-heat measurements. Magnetism in KU_2Te_6 is dominated by a C_{2v} point-group CEF splitting the U^{4+} $J = 4$ manifold into a series of nine singlets arranged between 0–204 meV. At low temperature, no magnetic order is detected down to $T = 0.36$ K, consistent with weak magnetic exchange and a lack of charge carriers to couple

*Present address: Department of Chemistry, University of California, Berkeley, California 94720, USA.

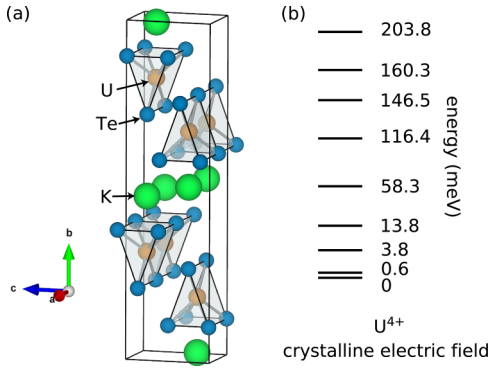

FIG. 1. (a) Crystal structure of KU_2Te_6 crystallizing in the *Cmcm* space group. KU_2Te_6 contains elongated trigonal prisms of UTe_6 in a local C_{2v} point group. (b) In KU_2Te_6, tetravalent uranium ions with total angular momentum $J = 4$ that splits into nine singlets in the local C_{2v} crystalline electric field. Energies of the singlets are extracted from crystalline electric field (CEF) fits to anisotropic magnetic susceptibility.

neighboring CEF singlets. Magnetism may develop via tuning the interaction strength, and its possible order parameters are discussed.

II. EXPERIMENTAL DETAILS

Single crystals of KU_2Te_6 were grown via the flux method in the elemental ratio U:K:Te of 1:1.4:4.5 [46,47]. Elements were placed in an alumina crucible equipped with a frit and catch crucible and subsequently sealed in a quartz ampule under vacuum [48]. The sample was initially heated to 375 °C and held there for 8 hours to allow for homogenization of the K-Te melt. Then, the sample was heated to 850 °C and held there for another 8 hours. Subsequently, the sample was slowly cooled to 500 °C at 10 °C/hr after which crystals were isolated via centrifugation. The resultant thin, malleable plate-like crystals were placed in an inert environment to reduce degradation due to atmospheric air and moisture.

Single-crystal x-ray diffraction was obtained on a Bruker D8 Venture single-crystal diffractometer equipped with Mo $K\alpha$ $\lambda = 0.71073$ Å radiation. These measurements of KU_2Te_6 produced 4113 reflections and were indexed to the *Cmcm* space group shared by structurally similar compounds within the $CsTh_2Te_6$ family [40–45]. Refinement of the data were analyzed in the APEX 3 software suite with the full matrix least squares method [49].

Electrical resistivity measurements were obtained in a Quantum Design Physical Properties Measurement System (PPMS). At high temperatures, electrical resistance was measured with a standard four-point probe configuration using a low-frequency AC resistance bridge. Below $T < 100$ K, a two-point DC method was used due to the large sample resistance. Specific-heat data between $T = 200$ K and $T = 2$ K were additionally collected on a PPMS with the quasi-adiabatic thermal relaxation technique.

Magnetization measurements were performed in a Quantum Design Magnetic Properties Measurement System (MPMS3) equipped with a $\mu_0 H = 7$ T magnet. Magnetic susceptibility from $T = 350$ to 2 K in a $\mu_0 H = 0.1$ kOe field and isothermal magnetization at $T = 2$ K were obtained with fields parallel and perpendicular to the crystallographic b axis.

III. RESULTS AND DISCUSSION

KU_2Te_6 crystallizes in the *Cmcm* space group belonging to the $CsTh_2Te_6$ structure type. Refined single-crystal x-ray diffraction lattice parameters at room temperature reveal $a = 4.2465(14)$ Å, $b = 23.767(7)$ Å, and $c = 6.0934(15)$ Å, as shown in Fig. 1. In structurally similar KTh_2Te_6, half K occupancy was reported [41]. However, due to malleability of KU_2Te_6, we were unable to perform a full structural refinement, and our results cannot determine the occupancy at the K site. Locally, the U ions are surrounded by six Te in a distorted trigonal prism stretched along the b axis with local C_{2v} point-group symmetry. Nearest-neighbor U-U are separated by 4.25 Å, forming infinite one-dimensional chains along the a axis.

Specific heat as a function of temperature between 2 and 200 K is shown in Fig. 2(a), whereas Fig. 2(b) shows a zoomed-in view of the structural transition at $T_s = 48$ K for two different samples. Synthetic attempts of nonmagnetic analog KTh_2Te_6 were unsuccessful, and the specific heat due to lattice vibrations was therefore estimated with a Debye model with a Debye temperature of $\Theta_D = 165$ K. However, this model overestimates the specific heat near a feature at $T_s = 48$ K. To estimate the lattice contribution to specific heat near $T_s = 48$ K, a Debye model with two Debye temperatures of $\Theta_{D1} = 81$ K and $\Theta_{D2} = 193$ K was utilized in Fig. 2(b). Subtracting off the double Debye fit and integrating the entropy obtains a relatively small value of ≈9% of $Rln2$ between 30 and 55 K. This small amount of entropy loss is consistent with a weak structural transition and the absence of a concurrent transition in magnetic susceptibility in Fig. 3. As shown in Fig. 2(c), the low temperature $T = 2$–10 K portion of C_p/T was fit to $C_p/T = \gamma + \beta T^2$ to extract $\gamma = 4.74 \pm 1.01$ mJ K^{-2} mol^{-1} and $\beta = 8.84 \pm 0.04$ mJ mol^{-1}. In a clean insulator, the Sommerfeld coefficient γ is zero, which suggests KU_2Te_6 contains in-gap or impurity states. Correspondingly, β is related to the Debye temperature as

$$\Theta_D = \left(\frac{12\pi^4 n N_A k_B}{5\beta}\right)^{1/3}, \tag{1}$$

where n is the number of atoms, N_A is Avogadro's number, and k_B is Boltzmann's constant. In the low-temperature regime, this corresponds to $\Theta_{D,\beta} = 125$ K, in reasonable agreement with $\Theta_D = 165$ K from the Debye fit. In the high-temperature limit where $T \gg \Theta_{D,\beta}$, specific heat approaches the Dulong-Petit limit, where $C_p \sim 3Nk_B n = 224.5$ J K^{-1} mol^{-1}. This corresponds to $C_p/T \sim 1.12$ J K^{-2} mol^{-1} at $T = 200$ K, matching the experimental value in Fig. 2(a).

Resistivity versus temperature, shown in Fig. 2(d), reveals that KU_2Te_6 is insulating, in agreement with the low value of γ from the low-temperature specific-heat fit. The resistivity feature broadly observed near 50 K is a continuity of the spike more clearly observed in specific-heat data, and once again suggests a structural transition correlated to a change in electronic structure. It is possible that this structural transition is related to the superstructure observed charge-density-wave

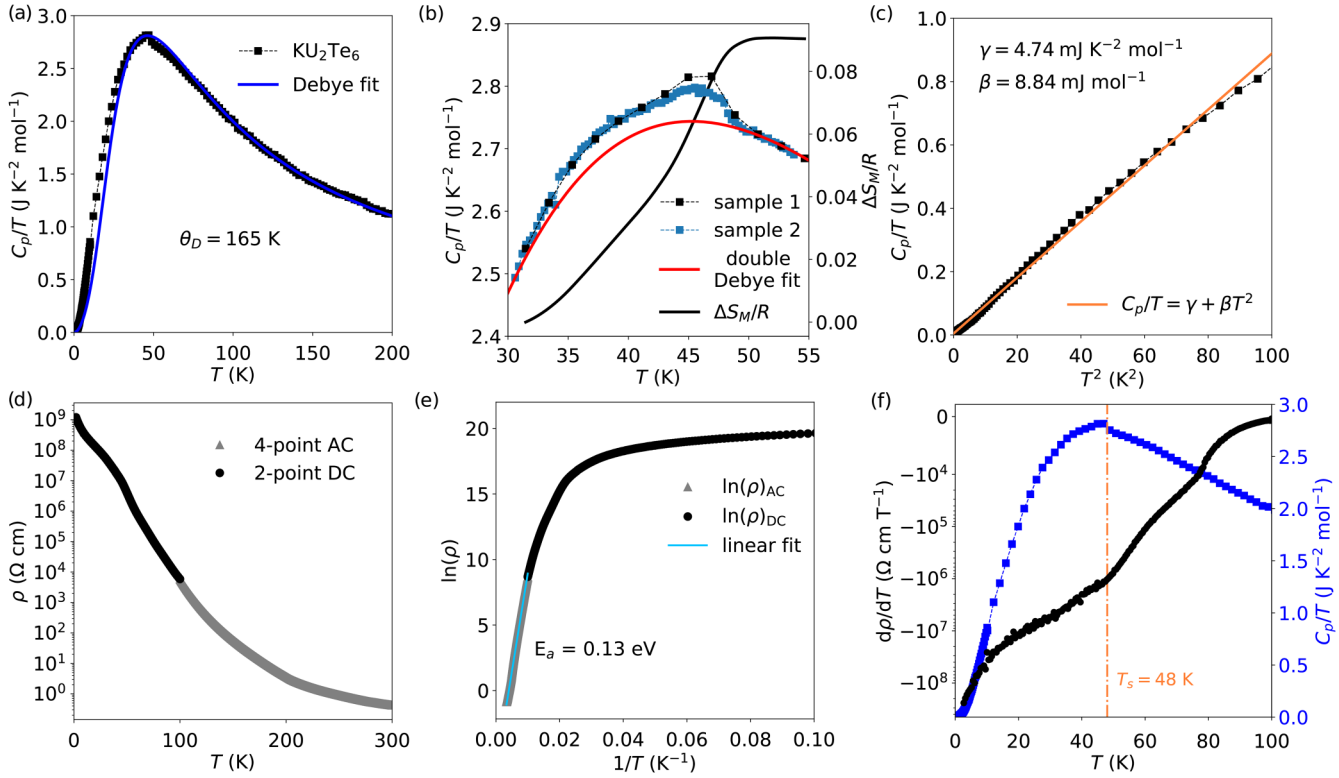

FIG. 2. (a) Specific heat of KU_2Te_6 collected between $T = 2$ to 200 K (black) overplotted with a Debye function (blue) approximating the lattice contribution to specific heat. (b) A weak transition appears near $T_s = 48$ K across multiple samples where the single Debye model overestimates the lattice specific heat. Integration of the entropy loss at the transition was estimated by subtracting a Debye model with two Debye temperatures and reveals only roughly 9% of $Rln2$ is released. (c) Low temperature $T = 2$ to 10 K fit (orange) of $C_p/T = \gamma + \beta T^2$, where $\gamma = 4.74 \pm 1.01$ mJ K^{-2} mol^{-1} and $\beta = 8.84 \pm 0.04$ mJ mol^{-1}. (d) Electrical resistivity (ρ) versus temperature (T) shows insulating behavior between $T = 2$ to 300 K. High-temperature data were collected with the standard four-point configuration (gray). Below $T = 100$ K, a two-point probe DC setup (black) was necessary to measure the resistivity of the sample. (e) Arrhenius plot $\ln(\rho)$ vs $1/T$ for KU_2Te_6 overlayed with a linear fit (blue) to the high-temperature data ($T > 100$ K). (f) Derivative of electrical resistivity $d\rho/dT$ reveals an inflection near $T_s = 48$ K concurrent with the transition observed in overplotted specific-heat data.

ATh_2Se_6 derived from Se-Se bonding and a $4a \times 4b$ superstructure [50]. A similar phenomenon could appear in KU_2Te_6 with Te-Te bonding along the c axis, but such a subtle structural change will require high-resolution probes, such as electron diffraction or pair distribution function analysis, as was similarly required for ATh_2Se_6 [50].

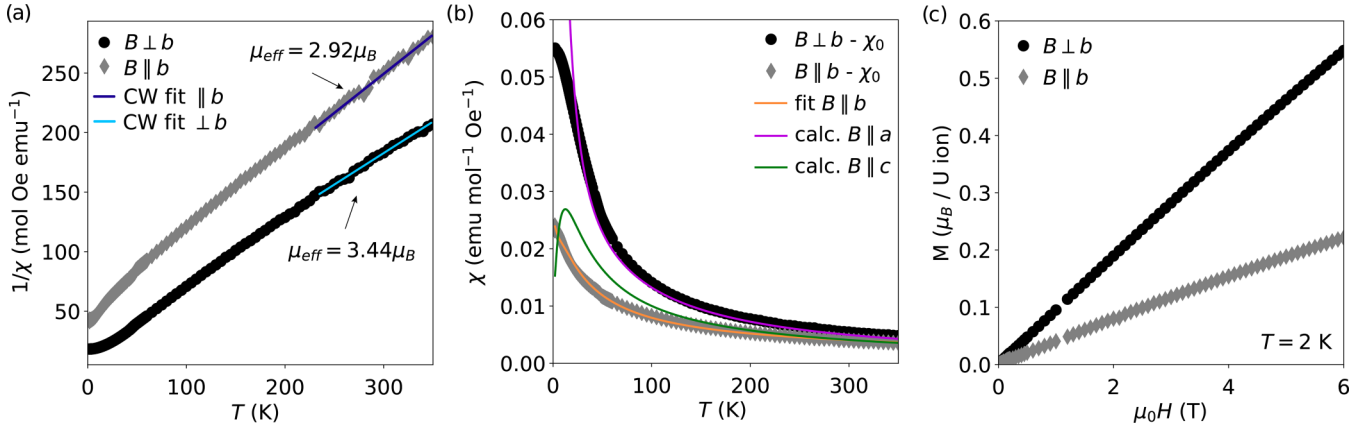

FIG. 3. (a) Anisotropic temperature dependent inverse magnetic susceptibility $1/\chi$ (T) with a field of $\mu_0 H = 0.1$ kOe applied both parallel (gray) and perpendicular (black) to the crystallographic b axis. Inverse magnetic susceptibility follows a Curie-Weiss law at high temperatures ($T > 225$ K) used to extract the effective magnetic moment. (b) Calculated magnetic susceptibility $B \parallel b$ fit (orange) to the U^{4+} crystalline electric field (CEF) Hamiltonian alongside calculated CEF susceptibilities along the a (purple) and c axes (green). (c) Magnetization versus field for KU_2Te_6 displays nonsaturating behavior up to $\mu_0 H = 6$ T.

TABLE I. Crystalline electric-field (CEF) parameters determined from fits to $B \parallel b$ magnetic susceptibility data in Fig. 3. The eigenenergies of the nine CEF singlets are shown with their symmetry in Bethe (Mulliken) notation and corresponding wave-function components.

			$\lvert m_j\rangle$								
CEF parameters (meV)	Energy (meV)	Symmetry	$\lvert 4\rangle$	$\lvert 3\rangle$	$\lvert 2\rangle$	$\lvert 1\rangle$	$\lvert 0\rangle$	$\lvert -1\rangle$	$\lvert -2\rangle$	$\lvert -3\rangle$	$\lvert -4\rangle$
$B_0^2 = -1.130$	0	Γ_4 (B_2)	0	0.54	0	0.45	0	−0.45	0	−0.54	0
$B_2^2 = 0.8655$	0.6	Γ_1 (A_1)	0.56	0	−0.04	0	−0.61	0	−0.04	0	0.56
$B_0^4 = -0.0053$	3.8	Γ_2 (B_1)	0	0.57	0	−0.42	0	−0.42	0	0.57	0
$B_2^4 = 0.0407$	13.8	Γ_3 (A_2)	0.37	0	−0.60	0	0	0	0.60	0	−0.37
$B_4^4 = 0.4577$	58.3	Γ_3 (A_2)	0.60	0	0.37	0	0	0	−0.37	0	−0.60
$B_0^6 = 0.0008$	116.4	Γ_1 (A_1)	−0.42	0	0.14	0	−0.79	0	0.14	0	−0.42
$B_2^6 = 0.0030$	146.5	Γ_4 (B_2)	0	0.45	0	−0.54	0	0.54	0	−0.45	0
$B_4^6 = -0.0018$	160.3	Γ_2 (B_1)	0	0.42	0	0.57	0	0.57	0	0.42	0
$B_6^6 = 0.0000$	203.8	Γ_1 (A_1)	0.12	0	0.69	0	0.12	0	0.69	0	0.12

The activation energy extracted from the linear region of an Arrhenius plot in Fig. 2(e) is calculated as 0.13 eV. This value is consistent with typical activation energies reported for the AR_2Q_6 structure type, which are generally within the range of ≈0.1–0.2 eV [40,41,43,51]. In comparison, KU_2Te_6 has a smaller activation energy than KU_2Se_6 at 0.27 eV [51], likely due to decreased ionic character of Te relative to Se. Figure 2(f) reveals that the weak structural transition T_s in specific heat coincides with a change in slope of the resistivity, $d\rho/dT$.

To investigate the magnetic properties of KU_2Te_6, anisotropic magnetic susceptibility and isothermal magnetization data were collected parallel and perpendicular to the plate-like crystals. Laue diffraction identified the cleavable b axis to be perpendicular to the thin crystal plate faces, which is likely induced by layering of [UTe_3] and K along the b axis. However, due to severe malleability of the crystals, the crystallographic orientations parallel to the plate faces were indeterminable.

Nevertheless, magnetic properties were measured parallel and perpendicular to the b axis to gauge the anisotropy of the magnetic U ion environment. Magnetic susceptibility and isothermal magnetization in Fig. 3 reveal an anisotropic response that may be analyzed with the Curie-Weiss law and fit to a crystalline electric-field (CEF) Hamiltonian. High-temperature ($T > 225$ K) Curie-Weiss fits were performed parallel and perpendicular to the b axis inverse magnetic susceptibility data in Fig. 3(a), revealing extracted effective magnetic moments of $3.44\mu_B$ and $2.92\mu_B$, respectively. The moment value parallel to the b axis resides close to the expected value of $5f^2$ U^{4+} of $g_J\sqrt{J(J+1)} = 3.58\mu_B$, where $J = L - S = 4$ ($L = 5$, $S = 1$) and g_J is the Landé g factor. The expected value of $5f^3$ U^{3+} resides nearby at $3.62\mu_B$. However, U^{4+} coincides with the insulating behavior and expected charge balance in this structure type. The Curie-Weiss analysis can additionally determine mean-field interaction Θ_{CW} values with $\Theta_{CW,B\parallel b} = 25$ K and $\Theta_{CW,B\perp b} = 8$ K, but their exact magnitude is shifted due to curvature induced by CEF effects from the $J = 4$ manifold.

In fact, the majority of the magnetic susceptibility curvature in KU_2Te_6 between 2 to 350 K can be captured with a CEF Hamiltonian derived from the non-Kramers U^{4+} ion ($J = 4$) in a C_{2v} point group. The CEF Hamiltonian is written with CEF parameters B_n^m and Steven's operators $\hat{O}_m^n$ [52] as

$$H_{CEF} = B_2^0\hat{O}_2^0 + B_2^2\hat{O}_2^2 + B_4^0\hat{O}_4^0 + B_4^2\hat{O}_4^2 + B_4^4\hat{O}_4^4 + B_6^0\hat{O}_6^0 + B_6^2\hat{O}_6^2 + B_6^4\hat{O}_6^4 + B_6^6\hat{O}_6^6. \quad (2)$$

This CEF Hamiltonian produces nine CEF singlets, none of which are forced to be degenerate by time reversal or C_{2v} symmetry. The $B \parallel b$ data were fit to Eq. (2) in Fig. 3(b) via minimizing $X^2 = (\chi_{\text{calc}} - \chi_{obs})^2/\chi_{\text{calc}}$ with $X^2_{\text{red.}} = X^2/\nu = 8.5$, where ν is the number of data points. Fit CEF parameters to magnetic susceptibility were obtained following procedures outlined previously [53,54] with the MANTIDPLOT software suite [55]. Corresponding symmetries, energies, and wave-vector components are shown in Table I in the J, m_j basis. The energies range from 0 to 204 meV, indicating that the underestimated moment value from high-temperature Curie-Weiss fits relative to the entire $J = 4$ multiplet originates from partial thermal depopulation of CEF levels at $T = 350$ K and below.

In Fig. 3(b), the calculated CEF $B \parallel a$ and $B \parallel c$ are shown alongside the $B \parallel b$ fit, which shows that the $B \parallel a$ calculation closely resembles the $B \perp b$ $\chi(T)$ data. Though, as previously mentioned, the exact orientation of $B \perp b$ could not be precisely determined via Laue x-ray diffraction and could reside somewhere between the a and c axes.

Generally, a local moment in CEF-split J ions forms from either time-reversal protection of odd-integer spin Kramers ions, symmetry protected non-Kramers ions, or accidental degeneracy of multiplet states that couple to form an effective magnetic moment [56–65]. Even-integer spin ions in low-symmetry point groups, such as is found here in KU_2Te_6 with $J = 4$ in C_{2v}, can produce nondegenerate singlets that *individually* cannot carry a magnetic moment. If they did, the time-reversed state would necessarily have the same energy, forming a degenerate non-Kramers or Kramers doublet.

Induced mixing of nondegenerate CEF singlets can produce a measurable moment. This can occur as a result of external parameters such as magnetic field, pressure, or temperature populating excited states or altering the energetic level structure [34,59,66–68]. This is exemplified in KU_2Te_6 via temperature and magnetic field in Fig. 3. Additionally,

TABLE II. Order parameters within the first two possible quasi-doublets of KU_2Te_6 coupling the ground state Γ_4 singlet to the first (second) excited state Γ_1 (Γ_2) singlet. Bars over operators indicate summation with respect to all possible index permutations.

Quasi-doublet	Symmetry	Moment	Operator
$\Gamma_4 \otimes \Gamma_1$ (0.6 meV)	Γ_4	Dipole	J_y
		Quadrupole	$\overline{J_yJ_z}$
		Octupole	J_y^3
			$\overline{J_yJ_z^2}$
			$\overline{J_x^2J_y}$
$\Gamma_4 \otimes \Gamma_2$ (3.8 meV)	Γ_3	Quadrupole	$\overline{J_xJ_y}$
		Octupole	$\overline{J_xJ_yJ_z}$

internal parameters like magnetic exchange or Kondo can instigate coupling of neighboring singlets into quasidoublets that can carry a magnetic moment, as proposed in UPd_2Al_3 [69], UM_2Si_2 [22–25], and $PrRu_2Si_2$ [68,70].

These quasidoublets are capable of initiating long-range magnetic order in the absence of Kramers or non-Kramers degeneracy. For this coupling to form, magnetic exchange or Kondo must work in unison with the single-ion terms [12], and the energetic strength and symmetry of these internal parameters must match and satisfy singlet-singlet interactions. Order parameters of the resultant quasidoublet are contained within the decomposition $\Gamma_{s1} \otimes \Gamma_{s2}$, where Γ_{s1} (Γ_{s2}) denotes the irreducible representation of the first (second) singlet of the quasidoublet [12,59].

This quasidoublet process can be applied to the lowest-lying singlets of KU_2Te_6 to explain the absence of magnetic order by placing upper bounds on its magnetic exchange. Building from the ground state, the order parameters of possible quasidoublets in KU_2Te_6 form from $\Gamma_4 \otimes \Gamma_{1,2,3,4}$. However, the anticipated singlets of interest that require the smallest magnetic exchange or Kondo are the lowest lying Γ_4 (0 meV) coupled to Γ_1 (0.6 meV) or Γ_2 (3.8 meV). Their decompositions are $\Gamma_4 \otimes \Gamma_1 = \Gamma_4$ and $\Gamma_4 \otimes \Gamma_2 = \Gamma_3$, respectively. The supported order parameters up to octupolar are shown in Table II, and the lowest independent multipolar order parameter is a $\overline{J_xJ_y}$ quadrupole within $\Gamma_4 \otimes \Gamma_2$. We note that the typical Ising admixture of singlets into a quasidoublet with J_z, as in UM_2Si_2 and $PrRu_2Si_2$ [22–25,68,70], does not appear in the CEF scheme of KU_2Te_6 until $\Gamma_4 \otimes \Gamma_4 = \Gamma_1$ at 146.5 meV. This is two orders of magnitude outside of the bounds of magnetic exchange for KU_2Te_6.

No magnetic moment or thermodynamic transition is observed to $T = 0.36$ K in KU_2Te_6, suggesting that these order parameters are not activated by magnetic exchange or Kondo interactions. Therefore, compatible magnetic exchange or Kondo contained within $\Gamma_1 \otimes \Gamma_4$ (Γ_2) is less than ≈0.6 (3.8) meV primarily because of large U-U distances of >4 Å and a lack of charge carriers to mediate substantial exchange. Modifications of the local U^{4+} CEF environment with chemical substitutions, alkali-ion deintercalation, or pressure in principle could alter the singlet energy arrangement, strength of magnetic exchange, charge-carrier density, and induce magnetic order in KU_2Te_6 or a structurally related material. In particular, UTe_2 contains similar $5f^2$ uranium in a C_{2v} point group with significant Kondo and magnetic exchange, albeit with a different CEF scheme with Γ_1 as the ground state and Γ_2 (Γ_3) as the first (second) excited state [17–19]. Quasidoublets from $\Gamma_1 \otimes \Gamma_{2,3} = \Gamma_{2,3}$ may lead to correlated behavior in UTe_2. Overall, tuning the CEF interactions and electronic structure of non-Kramers uranium materials will lead to quasidoublet formation.

IV. CONCLUSIONS

KU_2Te_6 crystallizes in the *Cmcm* space group with infinite U-U chains along the *a* axis. A weak transition appears at $T_s = 48$ K in specific heat and resistivity but not in magnetic susceptibility, which suggests a subtle structural transition. The material is insulating and contains tetravalent U^{4+} ions with total angular momentum $J = 4$ in a C_{2v} crystalline electric-field point group. Neighboring ions split the $J = 4$ manifold into a series of nondegenerate crystalline electric-field singlets, and KU_2Te_6 does not order magnetically indicating magnetic exchange and Kondo are weak in this material.

ACKNOWLEDGMENTS

We are grateful to S. Lin for helpful discussions. This work was performed under the auspices of the U.S. Department of Energy, Office of Basic Energy Sciences, Division of Materials Science and Engineering. M.B. acknowledges support from the Laboratory Directed Research and Development program.

[1] A. Mesbah, J. Prakash, and J. A. Ibers, Overview of the crystal chemistry of the actinide chalcogenides: Incorporation of the alkaline-earth elements, Dalton Trans. **45**, 16067 (2016).

[2] E. Manos, M. G. Kanatzidis, and J. A. Ibers, Actinide chalcogenide compounds, in *The Chemistry of the Actinide and Transactinide Elements* (Springer, Dordrecht, The Netherlands, 2010), pp. 4005–4077.

[3] D. Damien and C. De Novion, Crystal chemistry and electronic structure of actinide compounds, J. Nucl. Mater. **100**, 167 (1981).

[4] C. H. de Novion, D. Damien, and H. Hubert, New ternary molybdenum chalcogenides $M_{1+x}Mo_6Se_8$, with M = Np, Pu, Am, J. Solid State Chem. **39**, 360 (1981).

[5] D. E. Bugaris and J. A. Ibers, Syntheses and characterization of some solid-state actinide (Th, U, Np) compounds, Dalton Trans. **39**, 5949 (2010).

[6] J. Prakash, A. Mesbah, J. Beard, S. Lebegue, C. D. Malliakas, and J. A. Ibers, Three new quaternary actinide chalcogenides Ba_2TiUTe_7, Ba_2CrUTe_7, and $Ba_2CrThTe_7$: Syntheses, crystal structures, transport properties, and theoretical studies, Inorg. Chem. (Washington, DC, US) **54**, 3688 (2015).

[7] A. Mesbah, J. Prakash, J. C. Beard, S. Lebegue, C. D. Malliakas, and J. A. Ibers, Four new actinide chalcogenides $Ba_2Cu_4USe_6$, $Ba_2Cu_2ThSe_5$, $Ba_2Cu_2USe_5$, and $Sr_2Cu_2US_5$: Crystal structures and physical properties, Inorg. Chem. (Washington, DC, US) **54**, 9138 (2015).

[8] F. Wedgewood and M. Kuzneitz, Actinide pnictides and chalcogenides. I. Study of magnetic ordering and ordered moments in uranium monochalcogenides by neutron diffraction, J. Phys. C: Solid State Phys. **5**, 3012 (1972).

[9] A. Cornelius, J. Schilling, O. Vogt, K. Mattenberger, and U. Benedict, High-pressure susceptibility studies on the ferromagnetic uranium monochalcogenides US, USe and UTe, J. Magn. Magn. Mater. **161**, 169 (1996).

[10] O. Vogt, Magnetization measurements on single crystals of uranium chalcogenides and pnictides, Physica B + C (Amsterdam) **102**, 206 (1980).

[11] A. Daoudi, J. Levet, M. Potel, and H. Noel, Crystal structure and magnetic properties of the hexagonal uranium dichalcogenides γUS_2 and γUSe_2, Mater. Res. Bull. **31**, 1213 (1996).

[12] P. Santini, S. Carretta, G. Amoretti, R. Caciuffo, N. Magnani, and G. H. Lander, Multipolar interactions in f-electron systems: The paradigm of actinide dioxides, Rev. Mod. Phys. **81**, 807 (2009).

[13] S. Ran, C. Eckberg, Q.-P. Ding, Y. Furukawa, T. Metz, S. R. Saha, I.-L. Liu, M. Zic, H. Kim, J. Paglione *et al.*, Nearly ferromagnetic spin-triplet superconductivity, Science **365**, 684 (2019).

[14] D. Aoki, A. Nakamura, F. Honda, D. Li, Y. Homma, Y. Shimizu, Y. J. Sato, G. Knebel, J.-P. Brison, A. Pourret *et al.*, Unconventional superconductivity in heavy fermion UTe_2, J. Phys. Soc. Jpn. **88**, 043702 (2019).

[15] S. Sundar, S. Gheidi, K. Akintola, A. M. Côté, S. R. Dunsiger, S. Ran, N. P. Butch, S. R. Saha, J. Paglione, and J. E. Sonier, Coexistence of ferromagnetic fluctuations and superconductivity in the actinide superconductor UTe_2, Phys. Rev. B **100**, 140502(R) (2019).

[16] S. Thomas, F. Santos, M. Christensen, T. Asaba, F. Ronning, J. Thompson, E. Bauer, R. Fernandes, G. Fabbris, and P. Rosa, Evidence for a pressure-induced antiferromagnetic quantum critical point in intermediate-valence UTe_2, Sci. Adv. **6**, eabc8709 (2020).

[17] P. F. Rosa, A. Weiland, S. S. Fender, B. L. Scott, F. Ronning, J. D. Thompson, E. D. Bauer, and S. M. Thomas, Single thermodynamic transition at 2 K in superconducting UTe_2 single crystals, Commun. Mater. **3**, 33 (2022).

[18] S. Liu, Y. Xu, E. C. Kotta, L. Miao, S. Ran, J. Paglione, N. P. Butch, J. D. Denlinger, Y.-D. Chuang, and L. A. Wray, Identifying f-electron symmetries of UTe_2 with O-edge resonant inelastic x-ray scattering, Phys. Rev. B **106**, L241111 (2022).

[19] S. Khmelevskyi, L. V. Pourovskii, and E. A. Tereshina-Chitrova, Structure of the normal state and origin of the Schottky anomaly in the correlated heavy-fermion superconductor UTe_2, Phys. Rev. B **107**, 214501 (2023).

[20] K. Kubo and T. Hotta, Influence of lattice structure on multipole interactions in Γ_3 non-kramers doublet systems, Phys. Rev. B **95**, 054425 (2017).

[21] S. B. Wilkins, R. Caciuffo, C. Detlefs, J. Rebizant, E. Colineau, F. Wastin, and G. H. Lander, Direct observation of electric-quadrupolar order in UO_2, Phys. Rev. B **73**, 060406(R) (2006).

[22] A. Amorese, M. Sundermann, B. Leedahl, A. Marino, D. Takegami, H. Gretarsson, A. Gloskovskii, C. Schlueter, M. W. Haverkort, Y. Huang *et al.*, From antiferromagnetic and hidden order to Pauli paramagnetism in UM_2Si_2 compounds with $5f$ electron duality, Proc. Natl. Acad. Sci. USA **117**, 30220 (2020).

[23] K. Haule and G. Kotliar, Complex Landau-Ginzburg theory of the hidden order in URu_2Si_2, Europhys. Lett. **89**, 57006 (2010).

[24] H. Kusunose and H. Harima, On the hidden order in URu_2Si_2–antiferro hexadecapole order and its consequences, J. Phys. Soc. Jpn. **80**, 084702 (2011).

[25] J. A. Mydosh and P. M. Oppeneer, Hidden order behaviour in URu_2Si_2 (a critical review of the status of hidden order in 2014), Philos. Mag. **94**, 3642 (2014).

[26] G. H. Lander and W. G. Stirling, Neutron-inelastic-scattering measurements on uranium antimonide, Phys. Rev. B **21**, 436 (1980).

[27] G. Amoretti, A. Blaise, R. Caciuffo, J. M. Fournier, M. T. Hutchings, R. Osborn, and A. D. Taylor, $5f$-electron states in uranium dioxide investigated using high-resolution neutron spectroscopy, Phys. Rev. B **40**, 1856 (1989).

[28] A. Murasik, Neutron scattering studies of uranium compounds, in *Crystalline Electric Field and Structural Effects in f-Electron Systems* (Springer, New York, NY, 1980), pp. 229–240.

[29] N. Tateiwa, N. Metoki, Y. Koike, N. Kimura, H. Aoki, and T. Komatsubara, Neutron scattering experiment on $U_3Pd_{20}Si_6$ II: Crystalline electric field and spin wave excitations, Phys. B (Amsterdam, Neth.) **312-313**, 894 (2002).

[30] G. J. Nieuwenhuys, Crystalline electric field effects in UPt_2Si_2 and URu_2Si_2, Phys. Rev. B **35**, 5260 (1987).

[31] H. Noel, Magnetic susceptibility of the uranium trichalcogenides US_3, USe_3 and UTe_3, J. Less-Common Met. **121**, 265 (1986).

[32] C. A. Hutchison, Jr. and G. A. Candela, Magnetic susceptibilities of uranium (IV) ions in cubic crystalline fields, J. Chem. Phys. **27**, 707 (1957).

[33] E. D. Bauer, C. Wang, V. R. Fanelli, J. M. Lawrence, E. A. Goremychkin, N. R. de Souza, F. Ronning, J. D. Thompson, A. V. Silhanek, V. Vildosola, A. M. Lobos, A. A. Aligia, S. Bobev, and J. L. Sarrao, Simplifying strong electronic correlations in uranium: Localized uranium heavy-fermion UM_2Zn_{20}(M = Co, Rh) compounds, Phys. Rev. B **78**, 115120 (2008).

[34] P. Santini and G. Amoretti, Crystal Field Model of the Magnetic Properties of URu_2Si_2, Phys. Rev. Lett. **73**, 1027 (1994).

[35] H. Masuda, T. Fujino, N. Sato, K. Yamada, and M. Wakeshima, Synthesis and crystal structure of alkali metal uranium sulfides, Li_2US_3 and Na_2US_3, J. Alloys Compd. **284**, 117 (1999).

[36] H. Masuda, T. Fujino, N. Sato, and K. Yamada, Electrical properties of Na_2US_3, $NaGdS_2$ and $NaLaS_2$, Mater. Res. Bull. **34**, 1291 (1999).

[37] K. Stöwe and S. Appel-Colbus, Die synthese und kristallstruktur von K_2UTe_3, Z. Anorg. Allg. Chem. **625**, 1647 (1999).

[38] A. Mesbah, G. N. Oh, B. J. Bellott, and J. A. Ibers, Synthesis and crystal structure of $Cs_2U_3Se_7$, Solid State Sci. **18**, 110 (2013).

[39] J. A. Cody and J. A. Ibers, Uranium tellurides: New one-and two-dimensional compounds $CsUTe_6$, $CsTiUTe_5$, $Cs_8Hf_5UTe_{30.6}$, and $CsCuUTe_3$, Inorg. Chem. (Washington, DC, US) **34**, 3165 (1995).

[40] J. A. Cody and J. A. Ibers, Synthesis and structure of the layered thorium telluride $CsTh_2Te_6$, Inorg. Chem. (Washington, DC, US) **35**, 3836 (1996).

[41] E. J. Wu, M. A. Pell, and J. A. Ibers, Synthesis and characterization of KTh_2SeE_6, KTh_2Te_6 and $CsTh_2Se_6$, J. Alloys Compd. **255**, 106 (1997).

[42] B. C. Chan, Z. Hulvey, K. D. Abney, and P. K. Dorhout, Synthesis and characterization of AU_2Se_6 (A = K, Cs), Inorg. Chem. (Washington, DC, US) **43**, 2453 (2004).

[43] D. E. Bugaris, D. M. Wells, J. Yao, S. Skanthakumar, R. G. Haire, L. Soderholm, and J. A. Ibers, Dichalcogenide bonding in seven alkali-metal actinide chalcogenides of the KTh_2Se_6 structure type, Inorg. Chem. (Washington, DC, US) **49**, 8381 (2010).

[44] A. Mesbah and J. A. Ibers, Caesium diuranium hexatelluride, Acta Cryst. E **68**, i76 (2012).

[45] M. A. Pell and J. A. Ibers, Layered ternary and quaternary metal chalcogenides, Chem. Ber. **130**, 1 (1997).

[46] P. C. Canfield and Z. Fisk, Growth of single crystals from metallic fluxes, Philos. Mag. B **65**, 1117 (1992).

[47] P. F. Rosa and Z. Fisk, Flux methods for growth of intermetallic single crystals, in *Crystal Growth of Intermetallics* (Walter de Gruyter, Berlin, Germany, 2019), p. 49.

[48] P. C. Canfield, T. Kong, U. S. Kaluarachchi, and N. H. Jo, Use of frit-disc crucibles for routine and exploratory solution growth of single crystalline samples, Philos. Mag. **96**, 84 (2016).

[49] APEX3 Crystallography Software Suite, Bruker AXS, Inc., Madison, USA (2016).

[50] K.-S. Choi, R. Patschke, S. J. Billinge, M. J. Waner, M. Dantus, and M. G. Kanatzidis, Charge density wave caused by reducing $ThSe_3$ by one electron. Superstructure and short-range order in ATh_2Se_6 (A = K, Rb) studied by x-ray diffraction, electron diffraction, and diffuse scattering, J. Am. Chem. Soc. **120**, 10706 (1998).

[51] H. Mizoguchi, D. Gray, F. Q. Huang, and J. A. Ibers, Structures and bonding in $K_{0.91}U_{1.79}S_6$ and KU_2Se_6, Inorg. Chem. (Washington, DC, US) **45**, 3307 (2006).

[52] K. Stevens, Matrix elements and operator equivalents connected with the magnetic properties of rare earth ions, Proc. Phys. Soc. London, Sect. A **65**, 209 (1952).

[53] M. M. Bordelon, C. Liu, L. Posthuma, P. M. Sarte, N. P. Butch, D. M. Pajerowski, A. Banerjee, L. Balents, and S. D. Wilson, Spin excitations in the frustrated triangular lattice antiferromagnet $NaYbO_2$, Phys. Rev. B **101**, 224427 (2020).

[54] M. M. Bordelon, C. Girod, F. Ronning, K. Rubi, N. Harrison, J. D. Thompson, C. dela Cruz, S. M. Thomas, E. D. Bauer, and P. F. S. Rosa, Interwoven atypical quantum states in $CeLiBi_2$, Phys. Rev. B **106**, 214433 (2022).

[55] O. Arnold, J.-C. Bilheux, J. Borreguero, A. Buts, S. I. Campbell, L. Chapon, M. Doucet, N. Draper, R. F. Leal, M. Gigg *et al.*, Mantid-Data analysis and visualization package for neutron scattering and μ SR experiments, Nucl. Instrum. Methods Phys. Res. Sect. A **764**, 156 (2014).

[56] S. Onoda and Y. Tanaka, Quantum fluctuations in the effective pseudospin-$\frac{1}{2}$ model for magnetic pyrochlore oxides, Phys. Rev. B **83**, 094411 (2011).

[57] L. Savary and L. Balents, Quantum spin liquids: A review, Rep. Prog. Phys. **80**, 016502 (2017).

[58] W. Witczak-Krempa, G. Chen, Y. B. Kim, and L. Balents, Correlated quantum phenomena in the strong spin-orbit regime, Annu. Rev. Condens. Matter Phys. **5**, 57 (2014).

[59] P. Fazekas, *Lecture Notes on Electron Correlation and Magnetism* (World Scientific, Singapore, 1999), Vol. 5.

[60] Y.-P. Huang, G. Chen, and M. Hermele, Quantum Spin Ices and Topological Phases from Dipolar-Octupolar Doublets on the Pyrochlore Lattice, Phys. Rev. Lett. **112**, 167203 (2014).

[61] Y.-D. Li, X. Wang, and G. Chen, Hidden multipolar orders of dipole-octupole doublets on a triangular lattice, Phys. Rev. B **94**, 201114(R) (2016).

[62] C. Liu, Y.-D. Li, and G. Chen, Selective measurements of intertwined multipolar orders: Non-kramers doublets on a triangular lattice, Phys. Rev. B **98**, 045119 (2018).

[63] I. Sashin, E. Goremychkin, A. Szytula, and E. Clementyev, Crystal electric field in $RAgSb_2$ (R = Ho, Er, Tm) intermetallic compounds, Cryst. Rep. **52**, 412 (2007).

[64] M. A. Khan, Q. Zhang, J.-K. Bao, R. S. Fishman, A. S. Botana, Y. Choi, G. Fabbris, D. Haskel, J. Singleton, and J. F. Mitchell, Steplike metamagnetic transitions in a honeycomb lattice antiferromagnet $Tb_2Ir_3Ga_9$, Phys. Rev. Mater. **3**, 114411 (2019).

[65] Y. Shen, C. Liu, Y. Qin, S. Shen, Y.-D. Li, R. Bewley, A. Schneidewind, G. Chen, and J. Zhao, Intertwined dipolar and multipolar order in the triangular-lattice magnet $TmMgGaO_4$, Nat. Commun. **10**, 4530 (2019).

[66] L. C. Lopes and B. Coqblin, Neutron-scattering spectra of noncubic cerium Kondo compounds, Phys. Rev. B **38**, 6807 (1988).

[67] A. D. Christianson, E. D. Bauer, J. M. Lawrence, P. S. Riseborough, N. O. Moreno, P. G. Pagliuso, J. L. Sarrao, J. D. Thompson, E. A. Goremychkin, F. R. Trouw, M. P. Hehlen, and R. J. McQueeney, Crystalline electric field effects in $CeMIn_5$(M = Co, Rh, Ir): Superconductivity and the influence of Kondo spin fluctuations, Phys. Rev. B **70**, 134505 (2004).

[68] A. M. Mulders, A. Yaouanc, P. Dalmas de Réotier, P. C. M. Gubbens, A. A. Moolenaar, B. Fåk, E. Ressouche, K. Prokeš, A. A. Menovsky, and K. H. J. Buschow, $PrRu_2Si_2$: A giant anisotropic induced magnet with a singlet crystal-field ground state, Phys. Rev. B **56**, 8752 (1997).

[69] P. Thalmeier, Dual model for magnetic excitations and superconductivity in UPd_2Al_3, Eur. Phys. J. B. **27**, 29 (2002).

[70] R. Michalski, Z. Ropka, and R. Radwanski, Crystal-field interactions in $PrRu_2Si_2$, J. Phys.: Condens. Matter **12**, 7609 (2000).